Reorientations of the large-scale flow in turbulent convection in a cube

N. Foroozani,[1] J. J. Niemela,[1] V. Armenio,[2] and K. R. Sreenivasan[3]

[1]*International Centre for Theoretical Physics, Strada Costiera 11, 34151 Trieste, Italy*

[2]*Dipartimento di Ingegneria e Architettura, Università di Trieste, 34127 Trieste, Italy*

[3]*Departments of Physics and Mechanical and Aerospace Engineering, and the Courant Institute of Mathematical Sciences,
New York University, New York 10012, USA*

Large-eddy simulations of turbulent Rayleigh-Bénard convection were conducted for a fluid of Prandtl number Pr = 0.7 confined in a cube, for Rayleigh numbers of 10^6 and 10^8. The model solves the unsteady Navier-Stokes equations under the Boussinesq approximation, using a dynamic Smagorinsky model with a Lagrangian averaging technique for the subgrid terms. Under fully developed conditions the flow topology is characterized by a large-scale circulation (LSC) developing in a plane containing one of the diagonals of the cell, while two counter-rotating vortices consequently develop in the other diagonal plane, resulting in a strong inflow at the horizontal midplane. This flow structure is not static, with the LSC undergoing nonperiodic reorientations, or switching, between the two diagonal planes; hence, we supplement the observations of the three-dimensional time-averaged flow structures with single point measurements (time series) to shed light on the dynamics of the reorientations. For all observations, this switching results from a lateral rotation of the LSC in which some finite time spent in a transient state where the large-scale circulation is parallel to one set of side walls; there are, importantly, no observations consistent with so-called cessations of the LSC, in which it decays and then reforms in another plane without such a rotation. The average switching rate for the LSC is in excellent agreement with the results of Bai *et al.* [K. Bai, D. Ji, and E. Brown, Phys. Rev. E **93**, 023117 (2016)].

I. INTRODUCTION

Rayleigh-Bénard convection (RBC) is a simplified system with well-defined boundary conditions for studying the properties of thermal convection. Under conditions of turbulence, far from equilibrium, it provides a useful reference system, reproducing the essential physics, for flows present in more complex environments in nature and engineering applications. RBC consists of a fluid confined in a shallow layer heated from below and cooled from above. The system has been the subject of extensive theoretical, experimental, and numerical studies in recent years (for reviews, see Refs. [1–9]) but many facets of this flow are only partially understood, at least in fully developed turbulent flows.

Thermal convection occurs in response to the unstable density differences induced by an imposed temperature gradient, represented by a nondimensional Rayleigh number, $\text{Ra} = \alpha g \Delta T H^3 / \nu \kappa$, where α is the isobaric thermal expansion coefficient, g the acceleration of gravity, ΔT the temperature difference maintained across the fluid layer of height H, and ν and κ are respectively the kinematic viscosity and thermal diffusivity of the fluid. Ra is the principal control parameter for free convection flows. With increasing Ra, the laminar structures characteristic of the primary convection onset give way to the emission of plumes from increasingly thinner boundary layers at the heated horizontal surfaces. In confined cells at least, these thermal plumes cluster to form a coherent structure known as the large-scale circulation (LSC), or mean wind [3,10–12], with upwelling and downwelling flow on opposite sides of the container. The geometrical shape of the container, in addition to the aspect ratio between characteristic horizontal and vertical lengths, has a nonintuitive influence on statistical features of the turbulent flow, such as the scaling of

the root-mean-square (rms) fluctuations in the cell center (see, for example, Refs. [13,14]). It should not be surprising that the orientational properties of the LSC are also affected by the container shape. Most experiments and numerical simulations have been carried out in a cylindrical geometry of aspect ratio (e.g., of diameter to height for a cylinder) unity which has a quasi-two-dimensional (2D) single-roll structure with a finite width of approximately half the cell diameter [15]. A number of works have addressed the dynamics of LSC; for example, experimental work by Niemela *et al.* [10] and subsequent analysis by Sreenivasan *et al.* [3] demonstrated the switching of the direction of the LSC at a single point, but could not distinguish between azimuthal *rotations* of the flow and *cessations* in which the LSC slows to a stop and restarts in a new orientation without undergoing a rotation. In a later experiment, Brown *et al.* [5] studied the orientational motion of the wind using multiple temperature probes and showed that both cessation and azimuthal rotation exist, with the former being less frequent. Stringano and Verzicco [16] simulated convection in air in a cylinder of aspect ratio 1/2 and observed a single roll breaking into two counter-rotating rolls stack vertically. Breuer and Hansen [17] studied RBC for infinite Prandtl number, Pr, in a 2D numerical model in a box and observed reversals of the LSC for Rayleigh number Ra = 10^8. Further work by the same group provided a more detailed statistical analysis of the reversal mechanism [18]. There are other 2D numerical studies in a box that report the reversals of the LSC to be due to cessations [19] or due to the chaotic movement of rolls perpendicular to the roll axis [20]. Sugiyama *et al.* [21] performed both experiments and simulations for the width-to-height aspect ratio $\Gamma = 0.85$ in a (quasi-)2D rectangular geometry and found that the corner-flow rolls

play a crucial role in reversing the wind direction (see also Ref. [3]); recent experiments by Ni *et al.* [22] found that the main damping force of the LSC in a quasi-2D system is from the corner rolls rather than the viscous drag from the side walls. In a three-dimensional (3D) cubic box, there are few studies on the orientations of the LSC plane. This geometry does not have the azimuthal symmetry of cylindrical containers and the LSC is found in one or the other diagonals [1,13] although as we show below it may undergo reorientations between the two diagonal planes. The intermediate states are transient and the flow is never found to be stable over appreciable times in any nondiagonal orientation. In general, the stability of the LSC in cubic enclosures remains an open area of investigation for such turbulent flows [23], p. 93].

In this paper we use *wall-resolving* large-eddy simulation (LES) to investigate the problem. In LES the large-scale motions in the flow are solved directly, whereas the effects of the small-scale motions are parametrized. *Wall resolving* means that we directly resolve the momentum and thermal boundary layers as in direct numerical simulation (DNS). This class of simulation is also defined as *quasi-DNS* [24] and its computational cost scales like 2.5 power of the Reynolds number, Re, less steeply than that of a DNS ($\propto$Re$^{3.5}$) which attempts to resolve all scales present in the turbulent flow. Hence, LES requires less computational power than DNS and is suited for the long-time simulations reported in this paper. The specific LES code has been used in recent years for a number of challenging physical problems, among others, in transitional flows (see Ref. [25]) and in stratified flows (see Refs. [26,27]). Here, in order to be even closer to DNS than in our previous work [14], we increased the number of cells by a factor of 6 and in addition have run significantly longer simulations, aimed at the analysis of switching already suggested by our previous observations but not reported there prior to a more systematic investigation.

Though numerical simulations are limited both in attainable Ra and in duration of observations with respect to experiments, i.e., in number of LSC turnover times, the advantages are that full spatial information is available. In other words, there is a trade-off between *dynamics* and *structure*.

The goal of the present work is to gain a better understanding of the 3D flow structure in a cubic geometry through simulations and to simultaneously use numerical *experiments* to shed light on the reorientation dynamics of the LSC, acknowledging that the sampling is limited with respect to experiments in general. Combining the two provides a fuller picture of the specific turbulent regime present in square cross-sectional geometries (including cubes). We first introduce the numerical scheme and boundary conditions in Sec. II. In Sec. III we present the numerical results for the stable and transient flow configurations in a cube, as well as the reorientation dynamics of the LSC. Finally, we summarize our findings in Sec. IV.

II. FORMULATION OF THE PROBLEM

A. Numerical method

Large-eddy simulations of the Boussinesq form of the Navier-Stokes equations for incompressible flow were performed using a second-order nonstaggered finite difference scheme. Variables are filtered through application of a low-pass filter whose width is proportional to the cell size, $\bar{\Delta} = (\Delta_x \Delta_y \Delta_z)^{1/3}$. The filtered governing equations can be written as follows:

$$\frac{\partial \overline{u}_j}{\partial x_j} = 0, \tag{1}$$

$$\frac{\partial \overline{u}_i}{\partial t} + \frac{\partial \overline{u}_j \overline{u}_i}{\partial x_j} = -\frac{1}{\rho_0}\frac{\partial \overline{P}}{\partial x_i} + \nu \frac{\partial^2 \overline{u}_i}{\partial x_j \partial x_j} - \frac{\overline{\rho}}{\rho_0}g\delta_{i2} - \frac{\partial \tau_{ij}}{\partial x_j}, \tag{2}$$

$$\frac{\partial \overline{\rho}}{\partial t} + \frac{\partial \overline{u}_j \overline{\rho}}{\partial x_j} = k\frac{\partial^2 \overline{\rho}}{\partial x_j \partial x_j} - \frac{\partial \lambda_j}{\partial x_j}. \tag{3}$$

Here, the overbar represents the filtering operation, $\overline{u}_i$ is the velocity component in the i direction (namely u, v, and w), x_i is the spatial coordinate in the i direction with x_2 as the vertical (upward) direction, $\overline{P}$ is the pressure field, t is time, and δ_{ij} is the Kronecker symbol. τ_{ij} and λ_j are the subgrid-scale (SGS) stress tensor and the SGS heat flux, respectively. We assume that the density is a linear function of the temperature as $\rho = \rho_0[1 - \alpha(T - T_0)]$, where ρ_0 is the density at the reference temperature T_0.

B. The subgrid-scale models

Filtered equations (1)–(3), in space, lead to unknown SGS terms which represent the effect of the subgrid scales on the large-scale eddies and must be parametrized so as to resolve the large-scale motion. The SGS stresses appearing in the filtered Navier-Stokes equations are responsible for the occurrence of energy between the large-scale and the subgrid-scale eddies. The numerical solution of the governing equations largely follows the approach described by Meneveau *et al.* [28] and Armenio and Sarkar [26], so we provide only a brief summary here.

We use the Lagrangian dynamic eddy-viscosity model [28] to parametrize the SGS stress tensor,

$$\tau_{ij} = \overline{u_i u_j} - \overline{u}_i \overline{u}_j = -2C\overline{\Delta}^2|\overline{S}|\overline{S}_{ij}, \tag{4}$$

where $\overline{S}_{ij} = \frac{1}{2}(\frac{\partial \overline{u}_i}{\partial x_j} + \frac{\partial \overline{u}_j}{\partial x_i})$ is the strain rate tensor. The same procedure is employed to resolve SGS heat flux by Armenio and Sarkar [26]:

$$\lambda_j = \overline{u_j \rho} - \overline{u}_j \overline{\rho} = -C_\rho \overline{\Delta}^2|\overline{S}|\frac{\partial \overline{\rho}}{\partial x_j}. \tag{5}$$

Here C and C_ρ are the Smagorinsky coefficients evaluated through a procedure introduced by Germano *et al.* [29]. The procedure involves the introduction of an additional test filter denoted by $\widehat{\Delta} = 2\bar{\Delta}$. The model coefficient, C, in the SGS stress model is given by

$$C = \frac{\langle M_{ij} L_{ij} \rangle_A}{\langle M_{mn} M_{mn} \rangle_A}, \tag{6}$$

where in this case averaging is over the Lagrangian trajectories of the fluid particles, denoted by $\langle \cdots \rangle_A$ and

$$L_{ij} = \widehat{\overline{u}_i \overline{u}_j} - \widehat{\overline{u}}_i \widehat{\overline{u}}_j,$$

$$M_{ij} = 2\widehat{\overline{\Delta}^2|\overline{S}|\overline{S}_{ij}} - 2\widehat{\overline{\Delta}}^2|\widehat{\overline{S}}|\widehat{\overline{S}}_{ij}.$$
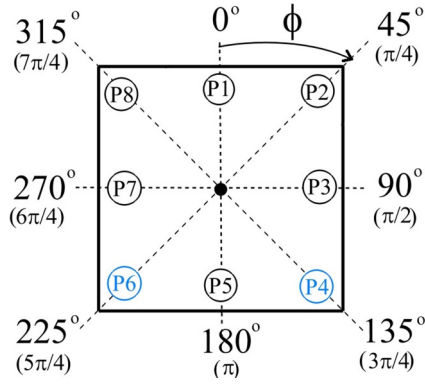
FIG. 1. Schematic of an arbitrary horizontal plane showing the azimuthal positions for probes, placed at azimuthal angles $\phi_i = (i\pi/4)$ ($i = 0, \ldots, 7$). The distance from the vertical walls is $0.1H$ for all cases. Probe positions P6 and P4 are shown in blue (grey in print) to help illustrate the positions for corresponding data shown below in Fig. 8.

The model coefficient, C_ρ, in the SGS heat flux model is given by

$$C_\rho = \frac{\langle \mathcal{I}_i \mathcal{M}_i \rangle_A}{\langle \mathcal{M}_k \mathcal{M}_k \rangle_A}, \qquad (7)$$

where

$$\mathcal{I}_i = \widehat{\bar{\rho} \widehat{u}_i} - \widehat{\bar{\rho}} \widehat{\widehat{u}}_i, \quad \mathcal{M}_i = 2\widehat{\bar{\Delta}^2 |\bar{S}|} \frac{\partial \bar{\rho}}{\partial x_i} - 2\widehat{\bar{\Delta}}^2 |\widehat{\bar{S}}| \widehat{\bar{S}}_{ij} \frac{\partial \widehat{\bar{\rho}}}{\partial x_i}.$$

The governing equations together with the density equation are solved using the semi-implicit, fractional-step algorithm developed by Zang *et al.* [30]. In our study, the Adams-Bashforth technique is used for the time advancement of the convective terms, whereas the diffusive terms are treated implicitly with the Crank-Nicolson scheme. The space derivatives are discretized with the second-order centered scheme; thus, the algorithm is overall second-order accurate in both time and space. The Poisson equation is solved using a multigrid method [31,32].

C. Computational domain and boundary conditions

In our study, the variables are made nondimensional by the height of the cube, H, as the length scale, free-fall velocity $U_f = \sqrt{\alpha g \Delta T H}$ as the velocity scale, and $\Delta\rho = \rho_t - \rho_b$ as the density scale, where the subscripts t and b refer to the top and bottom boundaries, respectively. Similar to some of the earlier experiments [5,33–35], we placed eight equally spaced probes around the azimuth at different heights into the

numerical Rayleigh-Bénard sample. The probes are located at $\phi_i = i\pi/4$ ($i = 0, \ldots, 7$) and vertical heights $y = 0.25H$, $0.5H$, and $0.75H$. All probes are spaced $0.1H$ from the vertical walls. A schematic diagram of the probes in any horizontal plane is depicted in Fig. 1. Note that the eddy turnover time can be defined as $T_{\text{eddy}} = 2H/v_{\text{rms}}$ [35], where v_{rms} is time average of the eight probes at midheight, $v_{\text{rms}} = (1/8) \sum_{i=1}^{8} (v_{\text{rms}}^i)$, with $v_{\text{rms}}^i(\mathbf{x}) = [\langle v(\mathbf{x})v(\mathbf{x}) \rangle_t - \langle v(\mathbf{x}) \rangle_t \langle v(\mathbf{x}) \rangle_t]^{1/2}$. Values of T_{eddy} for different Ra are listed in Table I. In this work, we also note that the LSC orientation can be determined with more precision from the vertical velocity profile than azimuthal temperature profile as pointed out by Stevens *et al.* [33].

Besides Ra, other control parameters are the Prandtl number, $\text{Pr} = \nu/\kappa$, and the characteristic width-to-height aspect ratio Γ. For confined convection, Γ does not sufficiently describe the geometry, since the geometrical shape of the container also plays a crucial role in the space-time evolution of the convective flow [13,14].

Since we solve the turbulent field down to the wall, no-slip conditions are used at all walls for the velocity; for the thermal field, adiabatic conditions are used at the vertical walls ($\partial \bar{\rho}/\partial \mathbf{n} = 0$, where $\mathbf{n}$ is the normal vector on surface) and isothermal conditions on the horizontal plates; the density difference $\Delta\rho/\rho_0 = 1$. The Prandtl number is set to $\text{Pr} = 0.7$ and we consider $\text{Ra} = 10^6$ and $\text{Ra} = 10^8$. The grid cells are clustered near all six walls to solve properly the momentum and thermal boundary layers ($\lambda_u, \lambda_\theta$). We estimate the mean thickness of the thermal boundary layer by $\bar{\lambda}_\theta = H/(2\text{Nu})$, where the Nusselt number (Nu) represents the dimensionless heat transfer [14], and ensure the number of grid points inside the thermal boundary layer (N_{BL}) to be greater than 3–5 (see Refs. [36,37] for a discussion). These grid points (N_{BL}) were chosen differently for different Ra to satisfy the above condition (see Table I).

We calculate the Nusselt number at the wall using Eq. (8), which is accurate at the second order (the error decreases with Δy^2). This is also consistent with the way the derivatives are calculated at the wall in the numerical method we use for the space-time integration of the Navier-Stokes equations. We note that the expression here is written for the bottom wall; a similar one also can be used for the top wall by symmetry. In practice we calculate Nusselt number at both walls and take the average:

$$\text{Nu}_b(x,z) = \frac{H}{\Delta\rho} \left(\frac{-8\rho_0 + 9\rho_1 - \rho_2}{3(\Delta y_1)} \right). \qquad (8)$$

Nusselt numbers obtained using Eq. (8) are shown in Table I. Note that we calculated the Nusselt number over 60 short time

TABLE I. Simulation parameters for $\text{Pr} = 0.7$, $\Gamma = 1$. N_x, N_y, and N_z are the number of grid points along x, y, and z directions; $\Delta_{\min}^y$, $\Delta_{\max}^y$, $\Delta_{\min}^x$, and $\Delta_{\max}^x$ are, respectively, the minimum and maximum grid spacing in the vertical y and horizontal x directions; N_{BL} is the number of grid points for solving the thermal boundary layer in conformity with Shishkina *et al.* [36] (actual resolution or requirement); the mean Nusselt number Nu represents the dimensionless heat transfer calculated over the top and bottom horizontal plane near the boundary; and $T_{\text{eddy}} = 2H/v_{\text{rms}}$ is the eddy-turnover time of the large-scale flow for different Ra.

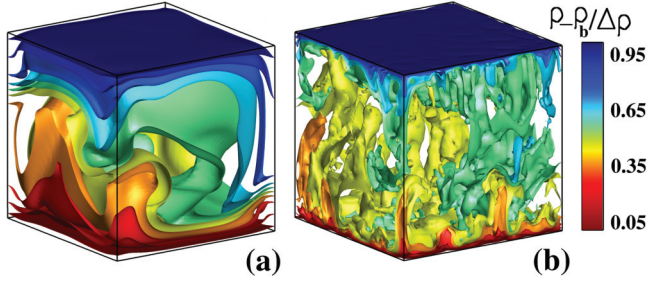| Ra	$N_x \times N_y \times N_z$	$\Delta_{\min}^y/H$	$\Delta_{\max}^y/H$	$\Delta_{\min}^x/H$	$\Delta_{\min}^x/H$	N_{BL}	Nu	T_{eddy}
10^6	$64 \times 96 \times 64$	1.7×10^{-3}	1.6×10^{-2}	1.5×10^{-3}	2.9×10^{-2}	12/2.8	8.1	12
10^8	$64 \times 96 \times 64$	7.4×10^{-4}	2.2×10^{-2}	1.3×10^{-3}	3.2×10^{-2}	6/5.5	31.6	7

FIG. 2. Instantaneous normalized density isosurfaces for (a) Ra = 10^6, (b) Ra = 10^8. Pr = 0.7, $\Gamma = 1$ with $64 \times 96 \times 64$ grids.

records of $350T_{\text{eddy}}$, each one, however, being of the same order as the total time used in the DNS study of Ref. [9]. For the main work presented here at Ra = 10^8, we obtain Nu = 31.6 ± 0.2, which includes values from DNS [9] within the error.

We use a hyperbolic tangent function to create stretching [38] in all directions. The minimum and maximum grid spacings in the vertical (Δ_{min}^y/H, Δ_{max}^y/H) and horizontal directions (Δ_{min}^x/H, Δ_{max}^x/H) are listed in Table I. We started our simulations from an interpolated turbulent field obtained from our prior work [14] with the grid of size $64 \times 96 \times 64 \approx 4 \times 10^5$. Note that these grid criteria are less restrictive than those used in DNS [39]. We let the simulation run for a certain number of eddy turnover times (say, ten) to make sure that we reached a statistically steady state, and from there we ran for another $1200T_{\text{eddy}}$ or so for accumulating statistics. This way, any dependence on initial conditions is lost. Indeed, the aim of this paper is to provide accurate characterization of the *temporal* evolution of the LSC structures over long periods of time. It should be stressed that, since the time interval over which the LSC is stable along any one diagonal at a given Ra is not constant, some care has to be taken during analysis of the observations. Throughout the paper (except for the Nu analysis), fields are averaged over finite time intervals in which reorientations are not observed to occur, unless stated otherwise.

The normalized instantaneous density isosurfaces obtained for two different Ra are shown in Fig. 2. This is qualitatively very similar to results from the DNS study of Ref. [40]. Indeed, the small plumes are clearly visible in Fig. 2(b), indicating that these important structures are resolved by our grid resolution. Further information on how the increase of Ra affects the size of flow structures is presented. It is clear that, even though the mean flow is similar in both cases, the regions of upflow on the left and the downflow on the right, as well as the size of the flow structures, decrease rapidly with increasing Ra.

III. RESULTS AND DISCUSSION

A. Flow topology

The 3D perspective of the flow observed in the cubic enclosure is shown in Fig. 3, which plots streamlines averaged *over a finite time* in which the orientation of the LSC is known to be stable. The color contour denotes the magnitude of the time-averaged vertical velocity $\langle v \rangle$. (Here $\langle \cdots \rangle$ denotes a time average of the quantity within the brackets.) The streamlines clearly show that the principal flow features are the
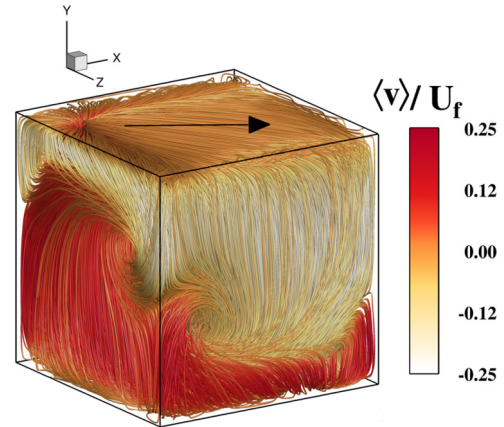

FIG. 3. Time-averaged velocity streamlines at Ra = 10^8, Pr = 0.7, and $\Gamma = 1$. The LSC is oriented along one of the diagonal directions as illustrated by the large arrow. The color coding (grey-scale in print) depicts the magnitude of the time-averaged vertical velocity normalized by the free-fall velocity $\langle v \rangle / U_f$.

LSC oriented along one of the vertical diagonal planes, and two counter-rotating vortices in the opposite plane, flowing inwards from the cell corner toward the cell interior and converging at the midheight position. We note that another feature of Fig. 3 is that the maximum amplitude of velocity, as a fraction of the free-fall velocity U_f, at Ra = 10^8 is roughly 0.25 at the midheight, in good agreement with Niemela *et al.* [10] in cylindrical containers. Similar features have been observed for Ra = 10^6 (see also Fig. 9).

In Fig. 4 we present a horizontal slice of the cube near the top boundary. The dark spot appearing in one or the other of the four corners is the impingement of the upward jet of plumes, comprising the LSC, on the top solid boundary before spreading out across the horizontal plane. Comparing the four panels in Figs. 4(a)–4(d) makes it clear that, even when the convection is statistically stationary, the LSC does not remain in the same orientation at all times; when it switches, the counter-rotating cells also change planes as a simple symmetry argument would suggest. Altogether, there can thus be four distinct stable flow states in principle, given the possibility of two different flow directions of the LSC stable in either of the two diagonal planes.

Whereas the LSC can change direction, sometime flowing down at a particular location along the vertical wall and sometimes flowing up at the same location, the counter-rotating cells have a fixed direction due to their origin from the spreading out of the LSC at the horizontal boundaries. That is, the flow is always downwards from the top and upwards from the bottom, along the sidewall, and therefore also always inwards toward the cell center, at the midheight where the two oppositely directed counter-rotating vortices converge (discussed further below).

Major reorientations of the LSC from one diagonal plane to the other occur nonperiodically in time; furthermore, the time over which the flow structure remains stable in any given diagonal orientation is not constant. For instance, for Ra = 10^8, the 3D structure of the flow field depicted in Fig. 4(a) is
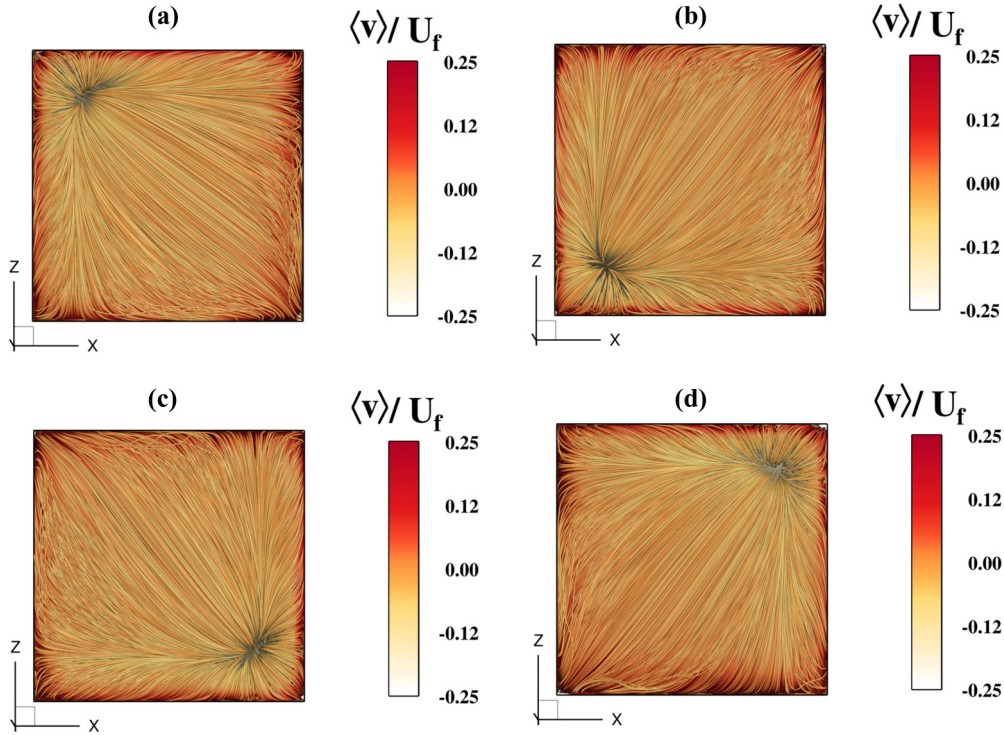
FIG. 4. Time-averaged velocity streamlines in a horizontal plane near the top boundary of the cube for $Ra = 10^8$, $Pr = 0.7$, and $\Gamma = 1$. The color coding (grey-scale in print) depicts the magnitude of the time-averaged vertical velocity normalized by the free-fall velocity $\langle v \rangle / U_f$. (a)–(d) Different instances in time, illustrating that the LSC does not remain fixed in its orientation.

the time-averaged result over $70 T_{\mathrm{eddy}}$, whereas the flow pattern shown in Fig. 4(b) is the time-averaged result of over $97 T_{\mathrm{eddy}}$.

In Fig. 5 we show the 3D perspective of the *transition* state of the global flow structure during a reorientation of the LSC from one stable diagonal plane to the other. Indeed, this transient state is always observed during reorientations and corresponds to a reorientation due to rotation of the LSC laterally rather than from cessations and restarting, for
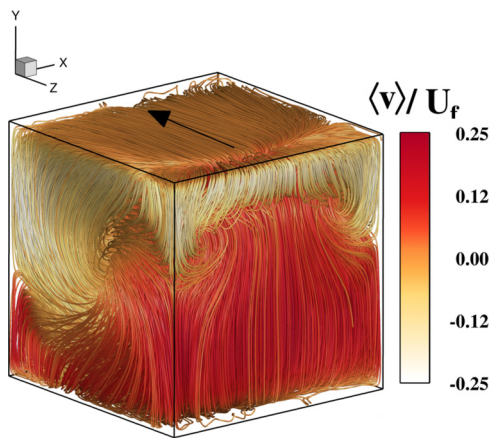

FIG. 5. Transient state during a reorientation of the LSC. Time-averaged velocity streamlines are shown for $Ra = 10^8$, $Pr = 0.7$, and $\Gamma = 1$. The color coding (grey-scale in print) depicts the magnitude of the time-averaged vertical velocity normalized by the free-fall velocity $\langle v \rangle / U_f$. The large arrow shows the direction of the LSC.

instance. We cannot rule out of course that the latter process would not be observed in a longer time record and/or with higher resolution. In the case shown the vertical velocity was averaged over about $25 T_{\mathrm{eddy}}$. To more clearly illustrate the global structure we show in Figs. 6(a)–6(c) three plane views of the transient flow. Rather than impinging at a spot, the contact of the LSC with the top and bottom boundaries occurs along an extended line. Hence, when the warm or cold fluid impinges the top or bottom plate [see Fig. 6(a)], *two* small back-eddies are formed in the adjacent corners rather than just one for the stable diagonal flow [see Fig. 6(b)]. Figure 6(c) shows the vortex structure induced in the vertical plane (zy) perpendicular to the LSC.

To better understand the stable flow structures occurring in a cubic geometry we refer to Fig. 7, where the arrows represent the time-averaged velocity vectors and the color contour shows the magnitude of the *horizontal* velocity computed as

$$\langle u_h \rangle = \sqrt{\langle u \rangle^2 + \langle w \rangle^2} \qquad (9)$$

in three different horizontal planes. Figures 7(a)–7(c) show, respectively, the plane near the bottom plate ($Y \approx 0.02 H$), near the top plate ($Y \approx 0.98 H$), and at the midheight ($Y \approx 0.5 H$). In all three panels of the figure the corners are assumed to be labeled as A (lower right), B (lower left), C (upper left), and D (upper right), though they are shown for clarity only in the first panel. In Fig. 7(a), we see clearly that the large-scale flow impinges at the bottom plate in a very localized spot close to corner A and spreads horizontally outward with the main flow extending to the opposite corner C while some flow also moves towards the other two corners, B and D,
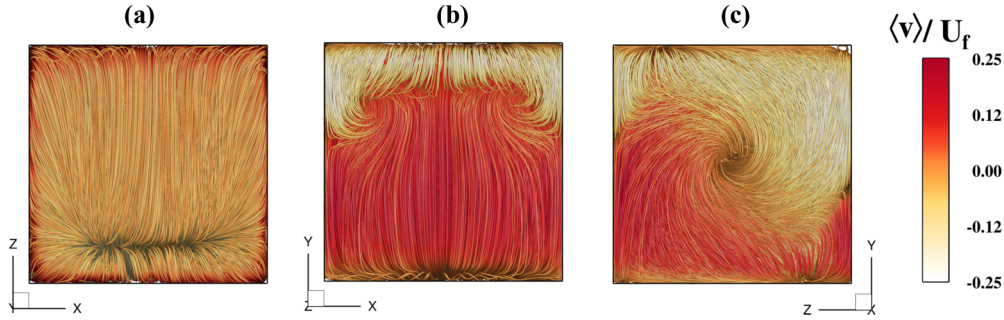
FIG. 6. Separated views for horizontal and vertical planes of Fig. 5 showing time-averaged velocity streamlines at Ra $= 10^8$, Pr $= 0.7$, and $\Gamma = 1$ in the transition mode. (a) Top panel, (b) vertical wall xy, and (c) vertical wall zy. The color coding (grey-scale in print) depicts the magnitude of the time-averaged vertical velocity normalized by the free-fall velocity $\langle v \rangle / U_f$.

as well as "behind" the impingement spot towards corner A. The latter gives rise to a back eddy. The mirror-symmetric situation happens at the top surface [Fig. 7(b)] where the impinging flow from the bottom occurs close to corner C, flowing mainly towards A, while also flowing towards the other three corners B, C, and D. This sets up another back eddy at C and the two horizontal flows at the top and bottom create the counter-rotating vortices in the opposite diagonal plane, i.e., that connecting corners B and D.

An interesting observation is shown in Fig. 7(c), representing the horizontal velocity in the cell midplane. Here we can see the horizontal inflow from corners B and D due to the counter-rotating vortices; it is also clear from the color coding that the vortices do not extend all the way to the center.

We should point out here that if we were to average over the entire time record, in order to obtain the Reynolds-averaging behavior, the resulting field would not be representative of the actual flow topology but instead gives a symmetric eight-roll pattern.

To obtain information on the *dynamics* of the reorientations of the flow, we perform numerical "experiments" by placing probes at fixed positions in the flow and examining the time series of various flow variables, much as in a physical experiment [41]. Referring to Fig. 1, probes 2 and 6 correspond to one of the vertical diagonal planes and probes 4 and 8 correspond to the opposite vertical diagonal plane. The other identifier refers to the horizontal plane, being above (u) or

below (d) the midplane (m), so that, e.g., location P6(u) refers to probe 6 in the horizontal plane at $Y = 0.75H$, while P2(d) refers to probe 2 at $Y = 0.25H$, and so on.

In Figs. 8(a)–8(d), we present time series of the normalized vertical velocity for Ra $= 10^8$. Figure 8(a) shows signals recorded from probes 4 and 8 at the midheight, i.e., probes P4(m) and P8(m). Referring to Fig. 1, these are the probes in the same vertical diagonal plane but on opposite sides of the cell, $\phi_i + \pi$. For the case when the LSC is in the same diagonal plane, the probes should show equal magnitude but opposite signs for the vertical velocity. We have isolated one of these instances by drawing a box around the signal where it occurs, at the normalized time of about $t \simeq 200$.

The LSC is seen to be in the same plane at other times in the series and it is clear that the duration of the LSC for these instances is not constant. Focusing on the top panel we see another signature that exhibits equal magnitude but zero mean and high variance for the velocity observed at both probes. This is precisely the signature we might expect in the presence of counter-rotating cells. Whereas the time average of the vertical velocity at the midplane, where the inflow occurs, must be zero (velocity entirely horizontally inward), the turbulent background ensures that the probe will sometimes see a negative flow of the upper vortex and sometimes a positive flow associated with the lower one giving rise to high variance. Looking at the entire time series at the midplane, then, we see an alternation between the vertical velocity
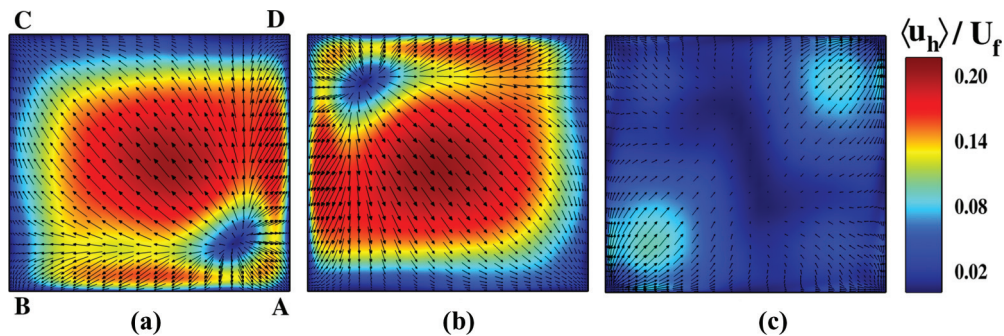

FIG. 7. 3D velocity vectors superimposed on the color-coded representation of the time-averaged, normalized time-averaged horizontal velocity $\langle u_h \rangle / U_f = \sqrt{\langle u \rangle^2 + \langle w \rangle^2}$ at Ra $= 10^8$, Pr $= 0.7$, and $\Gamma = 1$: (a) horizontal plane near the bottom boundary at $Y \approx 0.02H$, (b) horizontal plane near the top boundary at $Y \approx 0.98H$, and (c) horizontal plane at midheight at $Y = 0.5H$. In (a) we label the corners A–D for clarity of the discussion (see text). This same labeling is implied in the other two plots.
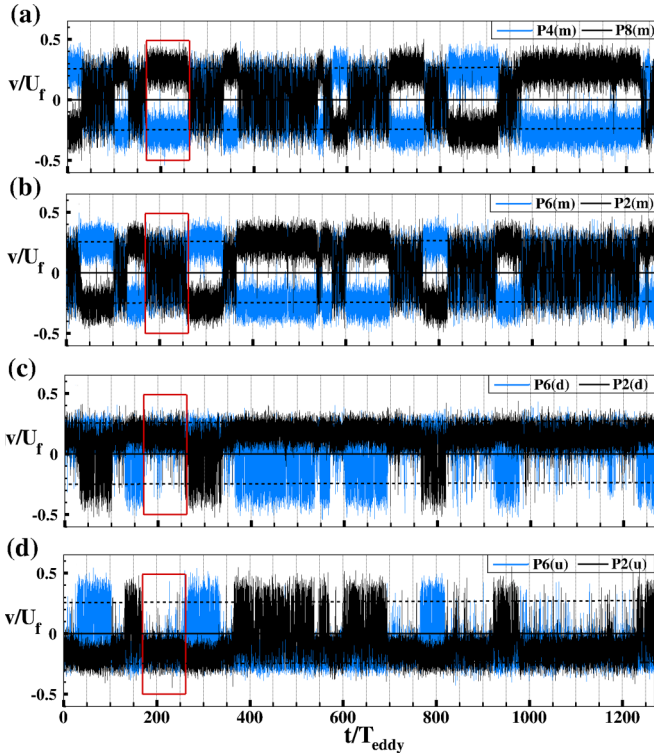
FIG. 8. Time series of vertical velocity for different "probe" positions. Positions P4 and P6 are in blue (grey in print), corresponding to the placement shown in Fig. 1. (a) Probes P4(m) and P8(m) at midheight, (b) probes P6(m) and P2(m) at the midheight at the opposite diagonal, (c) probes P6(d) and P2(d) at a distance of one-quarter of the cell height from the bottom, and (d) probes P6(u) and P2(u) at a distance of one-quarter of the cell height from the top. The solid horizontal line shows the position of zero-velocity magnitude and the boxed regimes highlight a particular part of the simultaneous time series, illustrating the different flow regimes occurring on opposite diagonals (LSC or counter-rotating vortices). The dashed lines in (a) and (b) illustrate the mean values for each probe. Ra $= 10^8$, Pr $= 0.7$, and $\Gamma = 1$. See text for nomenclature and the interpretation of these signals.

measured at the two positions having opposite sign and roughly equal magnitude, characteristic of the LSC, and zero mean with high variance, characteristic of the counter-rotating cells. The opposite situation is observed simultaneously, of course, for the other set of probes, 6 and 2, in the midplane.

Figure 8(b) plots the vertical velocity from probes P6(m) and P2(m), situated in the opposite vertical diagonal plane in which probes P4(m) and P8(m) reside. Looking at the boxed region—covering precisely the same interval of time as that drawn in Fig. 8(a)—we see the signature of the counter-rotating cells. A quick glance at Fig. 8 shows that whenever the LSC is in one diagonal the counter-rotating vortices are in the other.

In Figs. 8(c) and 8(d), we also show the signals from probes corresponding to one of the vertical diagonal planes but situated in horizontal planes one-quarter of the cell height above the bottom plate and below the top plate, instead of at the midheight. It suffices to show only one set of probes: P6 and P2.
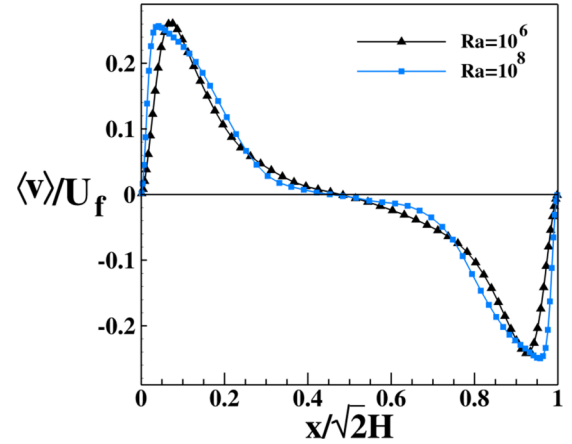

FIG. 9. Time-averaged vertical velocity normalized by free-fall velocity at the midheight as a function of diagonal distance at Ra $= 10^6$ (▲) and Ra $= 10^8$ (■), Pr $= 0.7$, and $\Gamma = 1$.

Figure 8(c) shows the time series obtained from probes placed in the lower plane at $Y = 0.25H$, while Fig. 8(d) corresponds to the upper horizontal plane at $Y = 0.75H$. Referring to the boxed regions (covering the same time interval as before, i.e., when the vertical plane containing probes P2 and P6 contains the counter-rotating vortices), we see that the flow is positive and of equal magnitude on opposite sides of the cell in Fig. 8(c) while the flow is negative and of equal magnitude in Fig. 8(d). Referring to Fig. 3, this signal is clearly understood. However, when the LSC is now in this same vertical diagonal plane, only one probe shows the expected magnitude and sign of the velocity while the other shows a signal with zero mean and large variance. This seemingly confusing signal arises simply because that probe is in the region of the back eddy (see Fig. 3). This illustrates that some probe placements in physical experiments can lead to signals that could be difficult to interpret.

Figure 9 displays the profile of the time-averaged vertical velocity at the midheight as a function of diagonal distance, i.e., measured from one corner to the opposite corner along a diagonal. The maximum velocity of LSC is roughly $0.25U_f$ in the region close to the corner and is zero at the center of the cell. Also note that, as Ra increases, the velocity peak shifts closer to the corner. In other words, the LSC becomes more squarish in shape, as was observed indirectly in the cylindrical, aspect ratio unity experiment of Niemela *et al.* [42].

B. A measure of the LSC reorientations

Following the work of Brown, Ahlers, and others [8,43–47], the orientation and strength of the LSC can be modeled by fitting the function

$$T_i = T_0 + \delta \cos(i\pi/4 - \phi) \quad (i = 0, \dots, 7) \quad (10)$$

to the temperatures recorded by the numerical probes at the midheight and the azimuthal position $\phi_i = i\pi/4$. Here, δ is a measure of the temperature amplitude of the LSC and ϕ is the azimuthal orientation of the LSC at midheight. An example of such a cosine fit (which we employ as an approximation
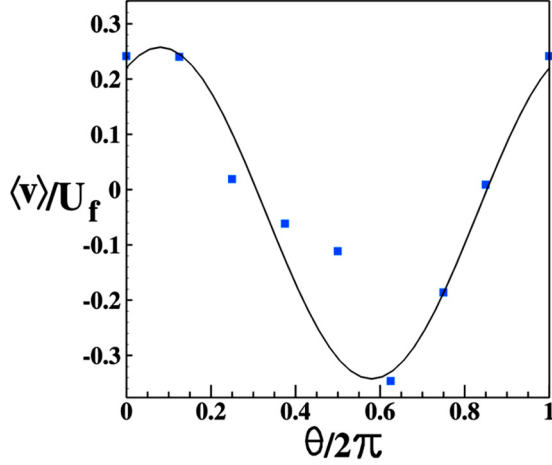
FIG. 10. Vertical velocity profile measured by the sidewall probes at the midplane for Ra = 10^8, Pr = 0.7, and $\Gamma = 1$. The solid black line shows a cosine fit of Eq. (10) to our data. The fit yields the orientation ϕ and an amplitude δ that describe the LSC.

for the square cross section) is shown in Fig. 10 with the eight equally azimuthally spaced probes at the midheight for Ra = 10^8 [45,46].

In order to gain a more complete understanding of the reorientations, we compute at each time t the azimuthal Fourier transform of the vertical velocities $v_i(t)$, where the subscript refers to a given probe position, similar to the work of Cioni *et al.* [34]. Thus, we obtain the phase ϕ and amplitude δ of the dipolar mode. The first Fourier components A_1 and B_1 are given by

$$\delta(t) = \sqrt{A_1^2 + B_1^2}, \quad \phi(t) = \text{sgn}(B_1) \arccos \frac{A_1}{|\delta|}, \quad (11)$$

where

$$A_1(t) = \frac{1}{2} \sum_{j=1}^{8} v_i(t) \cos \phi_i, \quad B_1(t) = \frac{1}{2} \sum_{j=1}^{8} v_i(t) \sin \phi_i.$$

$$(12)$$

In Fig. 11, we plot the strength $|\delta|$ and the phase ϕ of the first Fourier mode, which is a measure of the plane of the LSC.

In all the time series reported here, the change of LSC orientation (i.e., $\Delta\phi$) is $45° \leqslant \Delta\phi \leqslant 135°$. Importantly, we do not observe values of $180°$ corresponding to a reversal of flow direction in the same plane. The amplitude δ fluctuates around a mean value $\delta = 0.5U_f$ [see Fig. 11(a)]. As we saw earlier in Fig. 8, the boxed region near $t \simeq 200$ shows the LSC plane align along one of diagonal axes where P8 shows an upward flow direction (positive) and P4 shows downward flow (negative). It is clear that the LSC orientation is $135°$ as shown explicitly in the boxed region in Fig. 11(b).

Figure 12 shows a zoomed representation of a reorientation of the LSC with $\Delta\phi \approx 90°$ near $t \simeq 370$; note that δ does not vanish during the transition.

Comparison of the average switching rate for the LSC yields good agreement with the experimental results of Ref. [45]. Those authors quote a rate of 1.3×10^{-4} s^{-1} obtained for a continuous run of 21.7 days in which 251 events were observed. To compare with our results we need to normalize time and in this case we use natural units of the LSC turnover time which we define as the time for an advected "particle" to move a distance of $2H$. Those authors measure the speed of the LSC by the ratio of the distance between two vertically separated probes $H/4$ (where $H = 0.203$ m) to the time of peak correlation between their signals, which they measure as 16.6 ± 0.7 s. Therefore, the turnover time for their experiments, using the above definition, is 133 s. The switching rate observed by those authors is then 0.017 in normalized units of inverse time. For our numerical simulation we observe 20 events in 1250 normalized time units leading
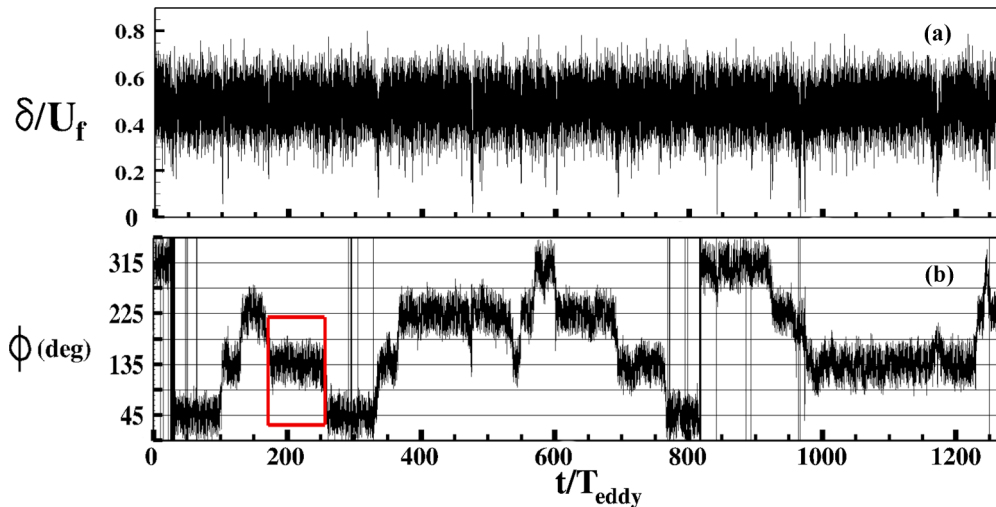

FIG. 11. Time series of (a) the amplitude δ and (b) phase ϕ of the first Fourier mode of the vertical velocity used as an approximate measure for the reorientation of the LSC, for Ra = 10^8, Pr = 0.7, and $\Gamma = 1$. The boxed region highlights one of the LSC orientations, $\phi \simeq 135°$ near $t \simeq 200$, corresponding to the same region boxed in Fig. 8. Nonperiodic switching of the LSC orientations between the corners is observed where $\Delta\phi < 180°$.
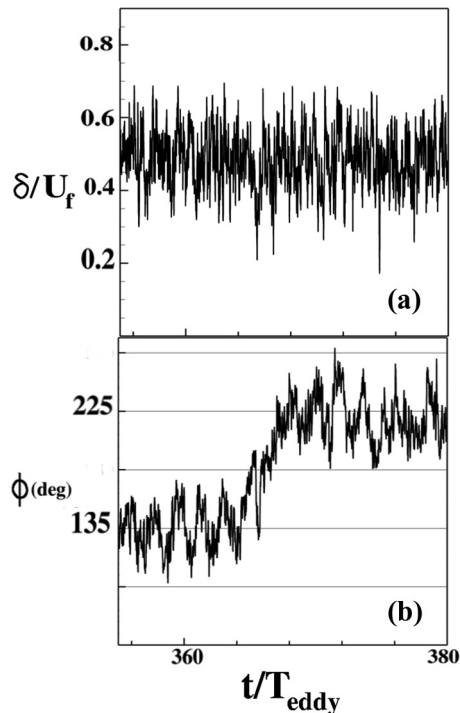
FIG. 12. Zoom of a switching event occurring near $t \simeq 370$. (a) Throughout this event δ is seen to remain nonzero and (b) $\Delta\phi \simeq 90°$ for $\mathrm{Ra} = 10^8$, $\mathrm{Pr} = 0.7$, and $\Gamma = 1$.

to a nondimensional switching rate of 0.016, in excellent agreement.

IV. SUMMARY AND CONCLUSIONS

In summary, we have computed turbulent convective flows confined within a cubic enclosure, using an LES scheme. The complete flow topology is computed, characterized by a LSC developing in one of the diagonal planes. Consequently, two counter-rotating vortices develop in the other diagonal plane, resulting in inflow at the horizontal midplane. This flow structure is not fixed in time as the LSC undergoes nonperiodic reorientations between the two diagonal planes. No other orientations are observed except for a transient state in which the LSC is oriented parallel to one set of sidewalls as it rotates laterally to its new stable position. In this context we do not observe any other switching scenario besides lateral rotation, such as cessation and reformation. We point out that long-time averaging, as in the Reynolds-averaging framework, leads to a nonphysical flow structure. Monitoring the vertical velocity at fixed points in the cell provides more insight on the dynamics of the reorientations and on the interpretation of signals corresponding to possible probe placement in physical experiments. Finally we note that the average switching rate of the LSC is in excellent agreement with the experimental observations of Bai *et al.* [45].

[1] X. L. Qiu and K. Q. Xia, Phys. Rev. E **58**, 486 (1998).

[2] J. J. Niemela, L. Skrbek, K. R. Sreenivasan, and R. J. Donnelly, Nature (London) **404**, 837 (2000).

[3] K. R. Sreenivasan, A. Bershadskii, and J. J. Niemela, Phys. Rev. E **65**, 056306 (2002).

[4] J. J. Niemela and K. R. Sreenivasan, J. Fluid Mech. **557**, 411 (2006).

[5] E. Brown and G. Ahlers, J. Fluid Mech. **568**, 351 (2006).

[6] R. Verzicco and K. R. Sreenivasan, J. Fluid Mech. **595**, 203 (2008).

[7] M. Kaczorowski and C. Wagner, J. Fluid Mech. **618**, 89 (2009).

[8] G. Ahlers, S. Grossmann, and D. Lohse, Rev. Mod. Phys. **81**, 503 (2009).

[9] M. Kaczorowski and K. Q. Xia, J. Fluid Mech. **722**, 596 (2013).

[10] J. J. Niemela, L. Skrbek, K. R. Sreenivasan, and R. J. Donnelly, J. Fluid Mech. **449**, 169 (2001).

[11] A. Parodi, J. von Hardenberg, G. Passoni, A. Provenzale, and E. A. Spiegel, Phys. Rev. Lett. **92**, 194503 (2004).

[12] B. A. Puthenveettil and J. H. Arakeri, J. Fluid Mech. **542**, 217 (2005).

[13] Z. A. Daya and R. E. Ecke, Phys. Rev. Lett. **87**, 184501 (2001).

[14] N. Foroozani, J. J. Niemela, V. Armenio, and K. R. Sreenivasan, Phys. Rev. E **90**, 063003 (2014).

[15] H. D. Xi, Q. Zhou, and K. Q. Xia, Phys. Rev. E **73**, 056312 (2006).

[16] G. Stringano and R. Verzicco, J. Fluid Mech. **548**, 1 (2006).

[17] M. Breuer and U. Hansen, Europhys. Lett. **86**, 24004 (2009).

[18] K. Petschel, M. Wilczek, M. Breuer, R. Friedrich, and U. Hansen, Phys. Rev. E **84**, 026309 (2011).

[19] U. Hansen, D. A. Yuen, and S. E. Kroening, Phys. Fluids A **2**, 2157 (1990).

[20] S. Paul, K. Kumar, M. K. Verma, D. Carati, A. De, and V. Eswaran, Pramana **74**, 75 (2010).

[21] K. Sugiyama, R. Ni, R. J. A. M Stevens, T. S. Chan, S. Q. Zhou, H. D. Xi, C. Sun, S. Grossmann, K. Q. Xia, and D. Lohse, Phys. Rev. Lett. **105**, 034503 (2010).

[22] R. Ni, S. D. Huang, and K. Q. Xia, J. Fluid Mech. **778**, 1 (2015).

[23] C. Sun, Y. H. Cheung, and K. Q. Xia, J. Fluid Mech. **605**, 79 (2008).

[24] P. R. Spalart, W. H. Jou, M. Strelets, and S. R. Allmaras, *Advances in DNS/LES: Proceedings of the First AFOSR International Conference on DNS/LES, Louisiana Tech University, Ruston, Louisiana, August 4-8, 1997* (Greyden Press, Columbus, OH, 1997).

[25] S. Salon, V. Armenio, and A. Crise, J. Fluid Mech. **570**, 253 (2007).

[26] V. Armenio and S. Sarkar, J. Fluid Mech. **459**, 1 (2002).

[27] J. R. Taylor, S. Sarkar, and V. Armenio, Phys. Fluids **17**, 116602 (2005).

[28] C. Meneveau, T. S. Lund, and W. H. Cabot, J. Fluid Mech. **319**, 353 (1996).

[29] M. Germano, U. Piomelli, P. Moin, and W. H. Cabot, Phys. Fluids A **3**, 1760 (1991).

[30] Y. Zang, R. L. Street, and J. Koseff, J. Comput. Phys. **114**, 18 (1994).

[31] V. Armenio and U. Piomelli, Flow Turbul. Combust. **65**, 51 (2000).

[32] L. Flacomer and V. Armenio, J. Turbul. **3**, N8 (2002).

[33] R. J. A. M. Stevens, H. J. H. Clercx, and D. Lohse, Phys. Fluids **23**, 095110 (2011).

[34] S. Cioni, S. Ciliberto, and J. Sommeria, J. Fluid Mech. **335**, 111 (1997).

[35] P. K. Mishra, A. K. De, M. K. Verma, and V. Eswaran, J. Fluid Mech. **668**, 480 (2011).

[36] O. Shishkina, R. Stevens, S. Grossmann, and D. Lohse, New J. Phys. **12**, 075022 (2010).

[37] R. Verzicco and R. Camussi, J. Fluid Mech. **477**, 19 (2003).

[38] M. Vinokur, J. Comput. Phys. **50**, 215 (1983).

[39] R. J. A. Stevens, R. Verzicco, and D. Lohse, J. Fluid Mech. **643**, 495 (2010).

[40] S. Wagner, O. Shishkina, and C. Wagner, J. Fluid Mech. **697**, 336 (2012).

[41] H. D. Xi and K. Q. Xia, Phys. Rev. E **78**, 036326 (2008).

[42] J. J. Niemela and K. R. Sreenivasan, J. Fluid Mech. **481**, 355 (2003).

[43] E. Brown and G. Ahlers, Phys. Fluids **18**, 125108 (2006).

[44] E. Brown and G. Ahlers, Phys. Fluids **20**, 075101 (2008).

[45] K. Bai, D. Ji, and E. Brown, Phys. Rev. E **93**, 023117 (2016).

[46] E. Brown and G. Ahlers, J. Fluid Mech. **638**, 383 (2009).

[47] E. Brown and G. Ahlers, Phys. Rev. Lett. **98**, 134501 (2007).